Using weak lensing in galaxy clusters to produce shear profiles & comparing the x-ray mass to the lensing mass

Andrea Minot
Brown University Department of Physics
Senior Thesis
Advisor: Ian Dell'Antonio

May 2020

1 Introduction

Galaxy clusters supply a plethora of astrophysical intrigue, ranging from the study of heavy elements, cosmological constraints, to dark matter. Because they are the largest gravitationally bound structures in the universe, their mass properties are of particular importance.

Many methods have been devised to estimate cluster masses including dynamical ones which rely on information about the velocity dispersion of the cluster members. as well as relations that involve the emission of x-ray by intergalactic gas [8]. These methods have their strengths and weaknesses, however, they all assume some physical or dynamical property which is not always entirely valid [8].

With the recent advancement of wide-field ground-based telescopes, it becomes increasingly beneficial to employ the technique of gravitational lensing to probe the mass characteristics of galaxy clusters. Lensing relies on the fact that light is bent in the presence of a gravitational field, and the amount of bending can be related to the mass of the object doing the bending. Lensing is particularly advantageous because it does not assume anything about the physical state of the cluster, giving an unbiased estimate of its mass distribution.

This being said, lensing does not come without drawbacks, the biggest being that performing lensing analyses are both time and computationally consuming. For this reason, astronomers hope to use combinations of mass-measuring techniques with the end goal of obtaining a scaling relation that can convert easily obtainable observables into an accurate mass estimate.

This is a long-term goal and will rely on the on-going and collaborative efforts of many research groups. For the scope of this project, 7 galaxy clusters will be investigated using weak gravitational lensing techniques. The matter distribution within the clusters will be explored as well as the cluster's x-ray emission distribution. Furthermore, the total cluster mass estimates obtained through lensing analysis will be compared to the mass estimated via x-ray luminosity.

2 Background

Einstein's theory of general relativity predicted that light would be deflected in a gravitational field. For a light beam which passes a point mass, M, which is at a distance ζ from the observer, is deflected by an angle, $\hat{\alpha}$.

$$\hat{\alpha} = \frac{4GM}{c^2\zeta} \tag{1}$$

Equation 1 is what is known as the deflection law and is valid as long as $\hat{\alpha} \ll 1$ which corresponds to cases with weak gravitational fields. In the case of lensing by anything other than black holes, this condition is satisfied.

This was proved in 1919 when the angle of deflection was measured of a background star during a solar eclipse. Although the measurement angle was only 30% accurate, it was enough to convince the scientific community. Now, we have measurements of this deflection angle with 5×10^{-4} precision [8].

In instances where the deflection is sufficiently strong, two images are produced. This constitutes strong gravitational lensing. The sun is not able to produce two images at once since its angular radius is far greater than the deflection angle.

2.1 Lensing Geometry

Before the specifics of this project are introduced, we must first discuss the basic geometry that describes gravitational lensing. Throughout this discussion, several approximations will be applied to simplify the mathematical descriptions of light being bent in the presence of a gravitational field. Let us imagine a scenario pictured in figure 1 where light rays are coming from a source and pass a mass concentration, referred to as the lens or the deflector, at a separation ζ. Firstly, it is true that as a wave packet travels from its source to an observer, the path, size, and cross section will be altered by all of the matter between the source and observer. However, we can assume that the dominant lensing affect happens at a single matter density location between the source and the observer. In other words, all of the deflection takes place at a single distance from the observer, denoted D_d in figure 1. This is referred to as the thin lens approximation and is only valid when the lens thickness is much less than the distance to the source. Luckily, this valid even for galaxy clusters whose thickness are approximately 1 Mpc, because the galaxies that serve as the sources are of order 1000 Mpc away from us [11].

Thus, we can assume that the lens lies on a plane referred to as the lens plane. Similarly, as shown in figure 1, the source being lensed is located in the source plane, and η is its true two-dimensional position. β is the corresponding true angular position of the source and

$$\beta = \frac{\eta}{D_s} \tag{2}$$

where D_s is the distance between the source and the observer. Similarly, ζ is the two-dimensional position of the light ray in the lens plane and θ is the corresponding angular position such that

$$\theta = \frac{\zeta}{D_d}. \tag{3}$$

Furthermore, $\hat{\alpha}$ is the deflection angle and depends on ζ. Another caveat to consider is that although D_{ds} is the distance from the lens plane to the source plane, $D_{ds} = D_s - D_d$ is only

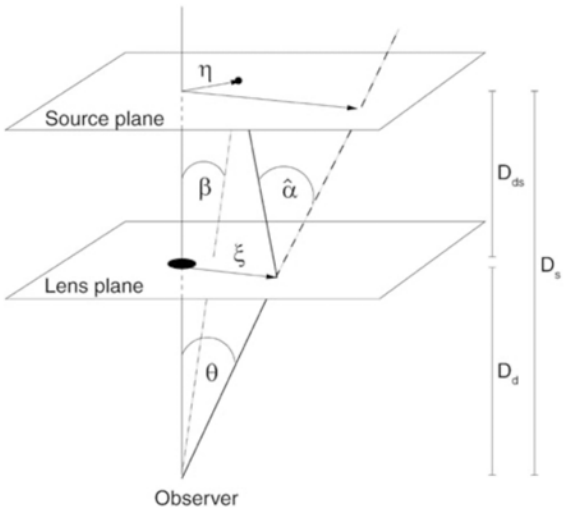

Figure 1: Shown is a simplified diagram of light originating from a source, D_s from an observer, being deflected by an angle $\hat{\alpha}$ due to a lens at a distance D_d from the observer. We are assuming that the thickness of the lens is much smaller than D_d and thus lies on a plane. (Adapted from: P. Schneider, J. Ehlers E.E. Falco 1992, Gravitational Lenses, Springer-Verlag).

valid so long as the distances are much less than c/H_0, the radius of the universe [8]. For our purposes, we will hold this definition of D_{ds} to be true.

Using the law of sines on the triangle in figure 1 made between the observer and the ends of vectors ζ and η,

$$\frac{sin(180-\hat{\alpha})}{D_s} = \frac{sin(\theta-\beta)}{D_{ds}} \tag{4}$$

and since all of the angles referenced are sufficiently small, $sin(\theta-\beta) \approx \theta-\beta$, and $sin(180-\hat{\alpha}) \approx 180-\hat{\alpha}$ [9]. This leads to what is referred to as the lens equation:

$$\beta = \theta - \frac{D_{ds}}{D_s}\hat{\alpha} \tag{5}$$

The deflection angle depends on the mass distribution of the lens, the simplest case being a point mass. We can rewrite the lens equation using equation for the deflection angle due to a point mass, given in equation 1 and the small angle approximation in equation 3.

$$\beta = \theta - \left(\frac{4GM}{c^2}\frac{D_{ds}}{D_d D_s}\right)\cdot\frac{1}{\theta} \tag{6}$$

Multiple images can be produced if the equation 5 has multiple solutions, θ_i. We can simplify the lens equation further to eventually solve for solutions, θ_i, by introducing a characteristic bending angle, θ_E, that only depends on the mass of the lens and the distances involved. This is sometimes referred to as the Einstein radius, and is given by

$$\theta_E = \left(\frac{4GM}{c^2}\frac{D_{ds}}{D_d D_s}\right)^{1/2} \tag{7}$$

so that

$$\beta = \theta - \frac{{\theta_E}^2}{\theta} \tag{8}$$

leading to the lens equation in quadratic form:

$$\theta^2 - \beta\theta - {\theta_E}^2 = 0 \tag{9}$$

with solution given by

$$\theta = \frac{1}{2}\left(\beta \pm \sqrt{4{\theta_E}^2 + \beta^2}\right). \tag{10}$$

If $\beta > \theta_E$, then the source will be weakly lensed and only one weakly distorted image will be produced. If $\beta < \theta_E$, then the source will be strongly lensed and multiple images will be produced.

Now, let us consider the case where the lens is a three-dimensional mass distribution rather than a point mass. The respective two-dimensional surface mass density distribution, $\Sigma(\zeta)$, can be obtained by projecting the density, $\rho(r)$, along the line of sight onto the lens plane.

$$\Sigma(\zeta) = \int_0^{D_s} \rho(r) dz \tag{11}$$

where r is a three-dimensional vector and ζ is the two-dimensional vector in the lens plane. The deflection law for a point mass shown in equation 1 can be rewritten by summing over all the mass elements in the lens plane

$$\hat{\alpha}(\zeta) = \frac{4G}{c^2} \int \frac{(\zeta - \zeta^{'})\Sigma(\zeta^{'})}{|\zeta - \zeta^{'}|^2} d^2\zeta^{'} \tag{12}$$

For a circle with constant surface density Σ, the deflection angle is given by

$$\hat{\alpha}(\zeta) = \frac{D_{ds}}{D_s}\frac{4G}{c^2}\frac{\Sigma\pi\zeta^2}{\zeta} \tag{13}$$

and using the small angle approximation for θ given by equation 3, this simplifies to

$$\hat{\alpha}(\theta) = \frac{4\pi G\Sigma}{c^2}\frac{D_d D_{ds}}{D_s}\theta. \tag{14}$$

We can define an important quantity known as the critical surface mass density, Σ_{crit}, which is given by the lens mass M distributed over the area of the Einstein ring,

$$\Sigma_{crit} = \frac{M}{{R_E}^2\pi} \tag{15}$$

where $R_E = \theta_E D_d$. We can plug in equation 7 and get

$$\Sigma_{crit} = \frac{c^2}{4\pi G}\frac{D_s}{D_d D_{ds}}. \tag{16}$$

Thus, if the mass density is constant with radius, the deflection angle in equation 14 can be simplified as

$$\hat{\alpha}(\theta) = \frac{\Sigma}{\Sigma_{crit}}\theta. \tag{17}$$

There are two important effects of lensing related to physical properties of the lens which we will focus on; magnification and distortion. These are respectively parameterized by the convergence, κ, and the shear, γ. The convergence is given by the ratio of surface mass density to critical surface mass density

$$\kappa \equiv \frac{\Sigma}{\Sigma_{crit}}. \tag{18}$$

This is the isotropic magnification of the image, and is also a good measure of whether the lensing is weak or strong [12]. If $\kappa > 1$, then the result is strong lensing. If $\kappa < 1$, the result is weak lensing.

Shear is a measure of the image's stretching in the tangential or azimuthal direction with respect to the lens. The value of γ depends on the mass distribution everywhere, not just at that position [12]. Thus, this quantity is nonlocal and in vector form,

$$\gamma_i = (\gamma cos(2\phi), \gamma sin(2\phi)) \,. \tag{19}$$

It also is important to note that both κ and γ can be calculated by taking the derivatives of the deflection. Thus, there exists an integral relation that allows one to calculate κ from γ, up to an additive constant.

2.2 Weak Lensing

Unlike in the strong lensing case, to measure the magnification or shear in the weak lensing case, we need independent knowledge of the source [12]. Thus, it becomes more beneficial to look at the general trend of many observed sources. In other words, in the case of weak lensing, we are interested in the statistical distribution of galaxy shapes. A good way to quantify galaxy shapes is with ellipticity, ϵ. In scalar form,

$$\epsilon = \frac{b^2 - a^2}{a^2 + b^2} \tag{20}$$

where a and b are the semimajor and semiminor axes, respectively. The ellipticity can also be represented in vector form as

$$e_i = (\epsilon cos(2\phi), \epsilon sin(2\phi)) = (e_+, e_\times) \tag{21}$$

where the two components of e_i are sometimes labelled as e_+ and $e_\times$, as shown in figure 2.

For an un-lensed distribution of galaxies, the cosmological principle demands that the ellipticities be random meaning that the observed distribution of e_i should be approximately gaussian with zero mean and a RMS of $\sigma_e \approx 0.3$ [12]. Any deviation from a mean of zero we can assume is caused by lensing.

The ellipticity of the image, ϵ^I, can be described in terms of the ellipticity of the source, ϵ_S, the shear, and the convergence:

$$\epsilon^I = \epsilon^S + \frac{2\gamma}{1 - \kappa} \tag{22}$$

Since we are looking at the average of ellipticities from many sources, we know that $< \epsilon^S >= 0$. Thus,

$$< \epsilon^I >= 2 < \frac{\gamma}{1 - \kappa} > \tag{23}$$

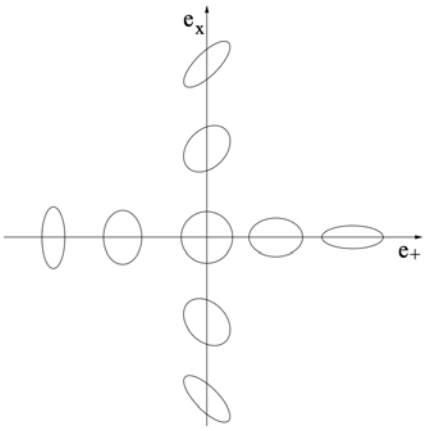

Figure 2: Ellipses with different amounts of ellipticity components, e_+ and e. (Figure retrieved from Wittman, 2002)

where the quantity on the right is the reduced shear, g [12]. We can make an approximation in the weak lensing limit when $\kappa \ll 1$, leading to

$$< \epsilon^I >= 2 < \gamma > \tag{24}$$

2.3 Galaxy Cluster Mass

Galaxy clusters are large gravitationally bound objects making them an ideal candidate for weak lensing [6]. We have just seen that the average image ellipticity of numerous background galaxies can be related to the shear caused by the lensing. Furthermore, the reduced shear $g = \frac{\gamma}{1-\kappa}$ can be measured giving an unbiased estimate for the projected mass density, κ, which is the Laplacian of the gravitational potential of the lens [5]. Thus, weak lensing is a direct method of obtaining the matter distribution of galaxy clusters.

Weak gravitational lensing has primarily been used to determine the mass distribution of medium-redshift galaxy clusters, however there exists some more traditional methods used to obtain this information [9]. Dynamical methods rely on line of sight velocity distributions measured of the cluster galaxies along with the virial theorem [9]. This method assumes that the cluster is in or near virial equilibrium, which is not always valid since the dynamical time scale of clusters is close in value to ${H_0}^{-1}$ and many observed clusters are still in the process of formation [9]. In addition, projection effects can further skew the measurements.

Another traditional method of obtaining matter distribution information about clusters is the method of diffuse x-ray gas emission. In particular, x-ray luminosity or x-ray temperature are utilized. For x-ray luminosity, the mass-luminosity relation is employed which realates the total x-ray luminosity (L_x) emitted via bremsstrahlung to the virial mass (M_{vir}):

$$L_x \propto {f_g}^2 {M_{vir}}^{4/3} \tag{25}$$

where $f_g = M_g/M_{vir}$ is the gas fraction [8]. The x-ray luminosity is usually measured over a certain energy interval, and for low energy photons below 2.4 keV such that $E_{photon} < k_B T$,

the x-ray luminosity becomes independent of T, yielding the relation

$$L_{2.4<keV} \propto {f_g}^2 M_{vir}[8]. \tag{26}$$

When tested with real cluster data, the slope obtained is closter to $L_{2.4<keV} \propto {M_{vir}}^{1.5}$ and can be explained by clusters where mechanisms of gas heating besides gravitational infall are present [8]. Thus, scatter exists in the x-ray luminosity-mass relation for clusters due to clusters for which hydrostatic equilibrium is not satisfied [8].

The temperature of the x-ray emitting intergalactic gas actually shows less scatter than the x-ray luminosity making it a better mass proxy than both x-ray luminosity and velcoity dispersion. The x-ray temperature, although preferred over x-ray luminosity as a cluster mass indicator, is significantly more difficult to obtain and relies on longer exposure times [8].

Gravitational lensing provides an alternative way of obtaining information about a cluster's mass distribution that does not rely on the physical state or nature of the cluster itself, however, it too suffers from various effect, the biggest being projection effects. Depending on the viewing angle, the observed cluster mass density can be skewed by up to a factor of two [2]. In addition, matter distributions between the source and cluster and cluster and observer will have effects on the measured amount lensing. Another drawback is that weak lensing analysis is a laborious process that involves many incremental steps. It is possible to get accurate mass information for clusters one at a time, but difficult to do for a large sample all at once.

2.4 Scaling Between X-ray Mass and Lensing Mass

Any of the above methods are prone to uncertainties and although lensing suffers the least, it is time-consuming and computationally intensive. To overcome this, one can employ the use of a scaling relation. In other words, a relation can be found between the cluster mass and some observable. Ideally, for a given mass, the scatter of the observable is small, making it a good mass proxy. For obtaining cluster masses, relations between x-ray temperature, x-ray luminosity, and virial mass are often utilized [8].

In the case of this study, we will be exploring the scale relation between the cluster mass obtained through weak lensing (lensing mass) and the mass obtained via x-ray luminosity (x-ray mass). A scaling relation between the lensing mass and the x-ray mass would not only account for the intrinsic scatter of both quantities, we could improve the more easily obtainable x-ray mass measurements using the more accurate lensing mass measurements. We will be using the x-ray luminosity masses given by the MCXC catalog shown in table 1. The luminosity-mass relation that was used in the MCXC catalog is given by:

$$L_{x500} \propto (M_{500})^{1.64}[7] \tag{27}$$

This relation relies entirely on calibration from clusters for which mass estimates are available which means the more clusters that are analyzed, the more accurate the scaling relation becomes. On this note, another factor to consider is selection bias. Since surveys are limited based on flux and thus for a given redshift, luminosity-limited, if a power law is fitted to this subset of objects, its slope will be biased relative to the underlying relation [8].

Name	α [hr min s]	δ [° ′ ″]	z	Lx_{500} [ergs s^{-1}]	M_{500} [$M_\odot$]	R_{500} [Mpc]
A3822	21 54 09.2	-57 51 19	0.0760	2.0979560e+44	3.04990e+14	0.9991
A2457	22 35 40.6	+01 28 18	0.0594	8.8252900e+43	1.81940e+14	0.8455
A3827	22 01 56.0	-59 56 58	0.0980	4.2044190e+44	4.58900e+14	1.1367
A3667	20 12 30.5	-56 49 55	0.0556	4.8719330e+44	5.16960e+14	1.1990
A3695	20 34 47.9	-35 48 48	0.0894	2.9630130e+44	3.72970e+14	1.0637
A3376	06 01 45.7	-39 59 34	0.0468	9.9663600e+43	1.97610e+14	0.8726
A0085	00 41 50.1	-09 18 07	0.0555	5.1000850e+44	5.31630e+14	1.2103
A1650	12 58 41.1	-01 45 25	0.0845	3.4706460e+44	4.12130e+14	1.1015
A3266	04 31 24.1	-61 26 38	0.0589	3.9773330e+44	4.55790e+14	1.1485

Table 1: Shown are the nine clusters involved in the analysis of this study. From left to right the quantities shown are the right ascension, declination, x-ray luminosity in the $0.1 - 2.4$ keV band, the total mass out to the R_{500} radius, and the standard characteristic radius. These measurements were obtained from the MCXC meta-catalog (see citation [7]).

2.5 Project Goals

In this study, nine galaxy clusters will be investigated as shown in table 1, however, priority will be given to Abell 3822 since most of the author's time was dedicated to this cluster in particular. In table 1, the right ascension (α), declination (δ), and redshift (z) are listed. In addition, properties were obtained from the MXCX meta-catalog which contains compiled properties of x-ray detected galaxy clusters [7]. These properties are the x-ray luminosity in the $0.1-2.4$ keV energy band (Lx_{500}), the total mass (M_{500}), and the standard characteristic radius (R_{500}). The subscript of 500 signifies that each parameter is referring to the extent of the cluster within which the mean overdensity is 500 times the critical density at the cluster redshift [7].

Below is a list of the goals for this study:

- Create a 2D mass density profile (approximate measure of a convergence map) for A3822 by measuring the shear of the lensed background galaxies.
- Obtain a cluster mass estimate by approximating the mass distribution of the cluster as a NFW profile and finding the mass of best fit.
- Plot the background galaxy ellipticity as a function of radius of the cluster (known as a shear profile).
- Visually compare the x-ray profile of A3822 to the mass density profile.
- Compare the x-ray masses (shown in table 1) to the obtained best fitted lensing mass.

3 Methodology

The methodology for this project is heavily based on data reduction and processing. Steps were followed according to the Large Synoptic Survey Telescope (LSST) Science Pipeline. In

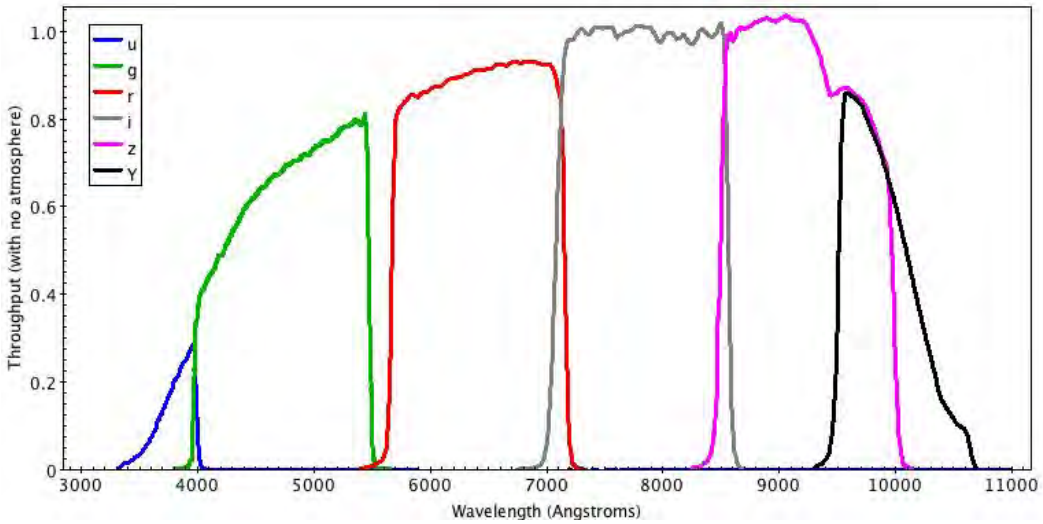

Figure 3: Shown are the bandpasses of DECam filters u, g, r, i, z, and Y assuming no atmospheric effects are present. (Image retrieved from ctio.noao.edu)

particular, the 2019 manual by Shenming Fu and Ian Dell'Antonio, "LSST Science Pipelines *obs_decam* Tutorial" was heavily relied on to complete this process (see citation [3]). The steps outlined in this pipeline are primarily used to process optical or near-infrared astronomical data. In the case of this project, we are using data from the Dark Energy Camera (DECam) which is a wide-field camera on the 4-meter Blanco Telescope at the Cerro Tololo Inter-American Observatory (CTIO) in Chile. DECam has several filters, u, g, r, i, z, and Y, and the corresponding bandpasses are shown in figure 3. In addition, DECam has a large field of view (FOV) spanning 2.2 degrees and a small pixel scale allowing the precise measurement of mass distributions of low-redshift galaxy clusters via weak gravitational lensing. DECam data is easily accessible on the National Optical Astronomy Observatory (NOAO) [1] Science Archive.

The methods taken to reduce and process the DECam data can be subdivided into five sections, retrieving the images, processing the single-exposure images, coadding single-exposure images, measuring the multi-band images, and lastly producing the final images and plots for analysis. These sections are broken up and outlined below.

3.1 Downloading Images

As mentioned previously, all raw images and calibration images were accessed from the NOAO Science Archive. The coordinates for the target cluster were inputted, as well as the telescope and instrument ("CTIO 4m + DECam imager") and all of the raw images in the available filters and from the available dates were downloaded. In the case of cluster A3822, filters g, r, u, z, Y, i, and VR were available, however the VR-band was omitted from the analysis. Then, calibration images from the corresponding dates (or within a few weeks of the date) must be retrieved, including both flat and bias (zero) frames. The flat frames aid

[1] It should be noted that NOAO recently joined with Gemini Observatory and LSST starting a new organization called "NSF's National Optical-Infrared Astronomy Research Laboratory".

in the correction of each pixel so that they are normalized to the same conversion between a quantity of light to electrical signal. We can divide our data by the flats to help remove image defects like field vignetting. The biases, capture the inherent readout noise of the sensor. Sometimes referred to as zeros because these frames have zero exposure time, the bias frames will be subtracted from the images to remove the bias levels from each pixel. It should also be noted that flats are filter-dependent while the biases are independent of filter.

All of this data was then downloaded to Brown University's Center for Computation and Visualization (CCV) remote server to allow for further analysis.

3.2 Processing Single-Exposure Images

Astrometry and photometry reference catalogs were determined and the portion of the catalog that contained the specified cluster was downloaded. The astrometry catalog provides accurate locations for objects in the FOV. For most clusters, including my analysis of A3822, Gaia Data Release 1 (DR1) is used for astrometry since it is able to provide high-precision information on the position of stars in the Milky Way with uncertainties less than 1 milliarcsecond (mas). However, we cannot use Gaia for photometry because it only uses 3 broad-pass filters. Instead, we use Pan-STARRS1 (PS1), Sloan Digital Sky Survey (SDSS) Data Release 9, or Sky Mapper to give us accurate flux information. PS1 uses the filters g, r, i, z, and Y, and covers sources with $\delta > -30°$. SDSS can be used for both astrometry and photometry and acts as a good compensate reference when either Gaia or PS1 do not exist. It uses filters u, g, r, i, z (slightly different than the filters of PS1) and has a precision of 0.1 arcseconds. In the case of southern hemisphere clusters like A3822, PS1 can be substituted with SkyMapper which has information for filters g, r, i, and z and spans approximate declinations of $0°$ to $-75°$. For cluster A3822, Gaia DR1 and SkyMapper were used for astrometry and photometry, respectively.

Next, the process of ingestion was performed. Ingestion is necessary to create a database with date and other specific information relevant to all of the data which can be referenced in later steps. In order, ingesting needs to be performed on the defects, fringes (bands Y and z), calibrations, and data images. This order is determined by performing the most error-prone ingestion first. Here, defects refer to a list of bad pixels that is the same for all cluster analyses and fringes are interference effects more present in redder bands, i.e. Y and z.

After ingestion has been completed, we move on to processing the data which involves detecting point spread functions (PSF) and thus sources, and calibrating the measurements. The input at this step are lists containing the exposures' visit ID numbers given in a particular syntax. This step requires the most processing time which makes it useful to divide up the lists by filter. The result are multi-extension Flexible Image Transport System (FITS) files created in each filter. An example of one of these FITS files produced for A3822 in the g-band is shown in figure 4. This is just a small portion of the entire FOV investigated for the cluster.

The last stage of processing the single-exposure images involves checking the quality of the data. Ideally, stars should have an ellipticity (ϵ) of zero and the boundary between their projected 2-dimensional surface and the black background of space should be well-defined. Thus, the PSF should be both narrow and sharp. We can evaluate the amount "fuzziness" by estimating the PSF of the stars as a gaussian and calculating the full width at half maximum (FWHM) which quantifies the width or spread of the distribution. Ideally, we

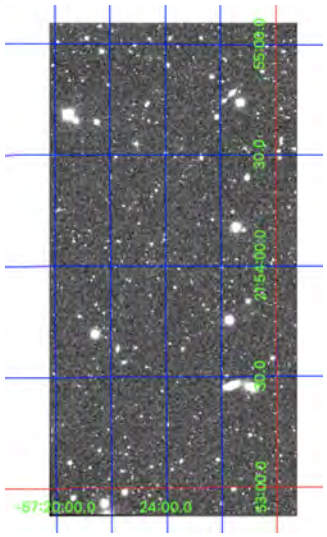

Figure 4: A resulting FITS file in the g filter produced after single-exposure processing was completed for cluster A3822. It should be noted that the axes are the RA and declination and this is only a single patch of the entire investigated FOV.

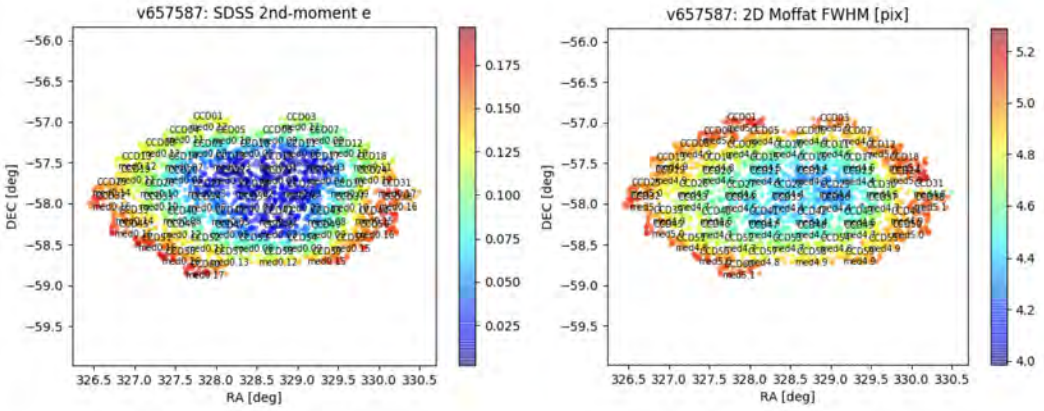

Figure 5: The CCD distribution for DECam. On the left, the color scale represents the measured ellipticity of stars. On the right, the color scale represents the measured full width at half max (FWHM) of the measured PSF of stars. Right ascension and declination are also displayed, corresponding to the region of sky that each CCD is observing. We see that the outer CCDs measure larger ellipticities and FWHMs introducing more error in these areas.

want our data to satisfy $\epsilon < 0.12$ and FWHM < 4.5. The output at this stage includes two plots showing DECam's arrangement of CCDs and their corresponding measurements of ellipticity and FWHM, shown on the left and right of figure 5. It should also be noted that the observed angular area on the sky by each CCD is represented by the axes in right ascension (RA) and declination (DEC) both in degrees.

In both plots in figure 5, it is apparent that the star observations made by outer CCDs corresponding to the outside edges of the images, have higher values meaning objects here will appear more elliptical and fuzzy.

In addition to these plots, this step outputs a text file listing the ID reference numbers to exposures that passed the quality-check and can therefore be used in later analyses.

3.3 Coadding Single-Exposure Images

Now, the process of coadding or stacking the images is introduced. The primary purpose of coaddition is to increase the signal-to-noise ratio of the sources. However, before coaddition, we must prepare what is known as a "skymap". A skymap is essentially a map of the celestial sphere and consists of an array of overlapping rectangular tracts. The individual tracts represent a curved projection, meaning they each have a different world coordinate system (WCS), however, the tracts' angular size is sufficiently small allowing us to approximate them as being flat. Each of these tracts can be subdivided into patches. The patches are arranged in a grid with each patch having an x-coordinate and y-coordinate ranging from 0 to 10. Since the outer edge CCDs introduce error (in terms of both ellipticity and PSF spread), we would expect the mid-ranged patches to be more reliable when used in analyses. Figure 6 shows a diagram of the celestial sphere and a (not to scale) patch. The exposure shown in the red box is patch 6,6 in the analysis of cluster A3822. Note that this is a centrally-located patch, and it approximately aligns with the center of the cluster which will be beneficial for lensing analyses later on since curtial measurements at the cluster center will be less likely biased due to distortions introduced by the CCDs. In whole, a skymap of tracts and patches is produced covering the same region that the processed images spans.

Next, joint-calibration is performed whereby different exposures are used on the same region of the sky to improve the astrometry and photometry calibrations. After this, these joint-calibrated processed exposures are warped onto the flat patches, creating temporary exposures to be used in coaddition. Lastly, the warped images are coadded giving the detected sources a higher signal-to-noise ratio. The coadded exposures have sources with cleaner shapes and more accurate flux information as compared to the single-exposures.

3.4 Multi-Band Measurements

The multi-band measurement stage involves detecting the sources in the coadded images, merging the detection catalogs from the different bands, de-blending the detected source, and measuring the shapes and fluxes of the source. Then the coadded measurements are merged, and the best measurement in each band is found to be used in the next step, forced photometry. The same sources are again measured but now in different bands at a fixed position and the shape is determined in the best chosen reference band.

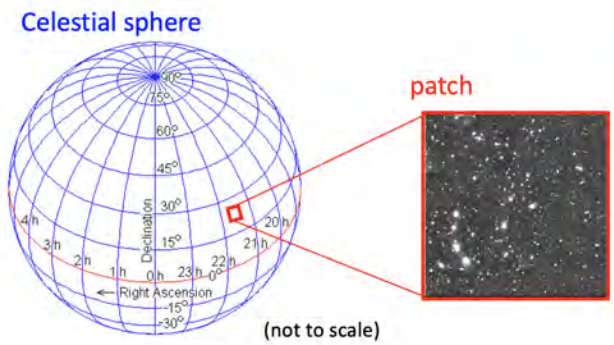

Figure 6: Shown is the celestial sphere in blue and a representative patch in red. The example exposure shown is patch 6,6 from cluster A3822 and was produced after the coaddition and multi-band measurement process was completed. It can be visually noted that this exposure contains less noise than the exposure before coaddition in figure 4. The patch size is not to scale, nor is the patch in the same location (RA and dec) as cluster A3822. Thus, this diagram should only be taken as a representative one.

3.5 Combining Patches & Obtaining Mass Characteristics

Now, with the multi-band measurements performed on all of the patches, we can select patches in a certain range (by specifying a min and max for the patch x-coordinate and y-coordinate) and "stitch" them back together. This results in a "whole" FITS file for each filter, spanning the specified patch range. With these whole FITS, we can combine different band combinations to make an RGB image. The end result of a igu-band RGB image is shown in figure 7, where the patches shown span from 3 to 8 in both the x and y direction.

Next, a two-dimensional mass density map for the cluster can be created which will act as an analog of the convergence. As a reminder, the shear (γ) is the anisotropic change in the light distribution of the background galaxies due to lensing and the convergence (κ) is the isotropic change in the light distribution of the background galaxies. The convergence can also be represented as the surface density of the lens (Σ) scaled by a factor Σ_{crit} which depends on the angular diameter distances between the observer, the lens, and the background galaxy. Therefore, we can study the mass distribution of the galaxy cluster (lens) by converting the measured reduced shear data into information about the convergence of the lens, assuming a cosmology and mean redshift for the background galaxies to approximate Σ_{crit}, and scaling the convergence field to a measurement the surface density of the lens. The conversion between the reduced shear and the convergence can be done using the fact that both κ and γ are second derivatives of the surface potential.

The convergence map that is produced is referred to as a "fiatmap" in our pipeline, and is essentially an array of values over the defined patch region. High values correspond to higher surface mass density and thus higher than average convergence, and lower values correspond to lower surface mass density and lower than average convergence. The fiatmap is created by statistically weighing each 2D location based on how sheared the background galaxies around that point. This works under the assumption that if background galaxies are significantly sheared around a given point, there must be a higher mass density at that

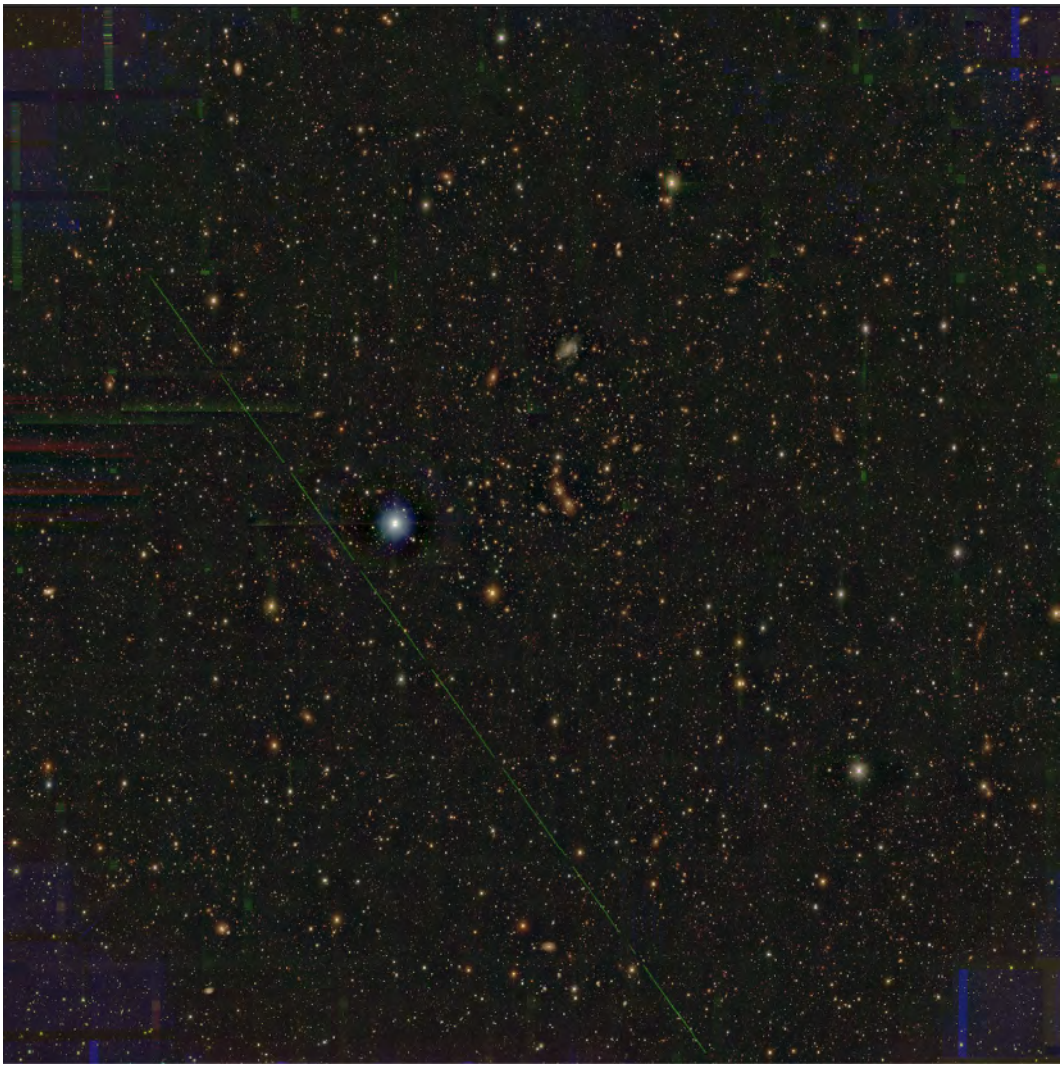

Figure 7: Shown is an RGB color image of cluster A3822, generated using filters i, g, and u. The patches shown range from 3 to 8, in both the x and y direction. The green streak is a satellite caught in the exposure and the colored distortions around the edges are due to failed biased subtractions.

point.

A "shear profile" is also generated which plots the tangential and cross component of the ellipticity of background galaxies as a function of radius from the center of the cluster. To generate a shear profile, the center of the cluster must be specified so that the shearing can be measured with respect to a center point. There are several ways of determining the center point of the cluster. Initially, it was determined by looking at the convergence map and visually noting the coordinates of the central-most bright signal. Then later it was determined using x-ray data from the NASA Extragalactic Database which used the ROSAT All Sky Survey.

Lastly, we will approximate the spatial mass distribution of the cluster as a Navarro-Frenk-White (NFW) profile. The NFW profile is commonly used to fit dark matter halos, however, it also serves as a good fit on average for galaxy clusters. With this NFW approximation, the shear profile can be used and a "best-fit" total NFW profile mass can be found. It should be noted that the NFW total mass is defined by integrating out to a radius within which the mean overdensity of the profile is 200 times the critical density.

4 Results

Approximately 8 clusters have been fully processed using the LSST pipeline, and more are to come. This being said, the author spent her time working with data from cluster A3822, while the other 8 clusters were processed by other researchers in the group. For this reason, individual cluster images shown in this section will be limited to that from A3822 and any other relevant cluster data can be referred to in the appendix.

4.1 Convergence and X-ray Distributions

It is well known that x-ray plasma in rich galaxy clusters make up 12% of the mass [1][10], while stellar mass makes up less than 1% [4]. Thus, we would expect the majority of the x-ray emitting gas to congregate at the center of the cluster where the gravitational potential well is the deepest. For this reason, x-ray emission data is particularly useful in determining the central region of galaxy clusters. Furthermore, comparing the distribution of x-ray emission to the surface density profile produced via lensing analysis can lend information on the cluster's morphology and evolution. In this study, however, we will be using the two in a qualitative context.

Shown in figure 8 on the left is the produced mass density profile for A3822 and on the right is Chandra x-ray data for the same cluster. Note that the density profile spans patches from 3 to 8 in the x and y directions meaning this angular area is much larger than that which the x-ray data spans. Both are in false-color and a colorbar was chosen arbitrarily based on what made the data visually distinct.

In figure 8, contours were derived from the convergence map and the x-ray data and overlaid on an irg color image of cluster A3822. The x-ray contours are shown in pink, and the convergence contours in blue. It is visually apparent that the cluster center in the x-ray data aligns with a peak in the convergence map, which is what we expect. This being said, the mass density map shows a significant amount of other areas with high convergence far from the cluster center. These are likely not actual regions of higher density, but rather noise due to increased error in the reduced shear measurements as the radius from the center increases. This is further supported by the fact that the peak in convergence that

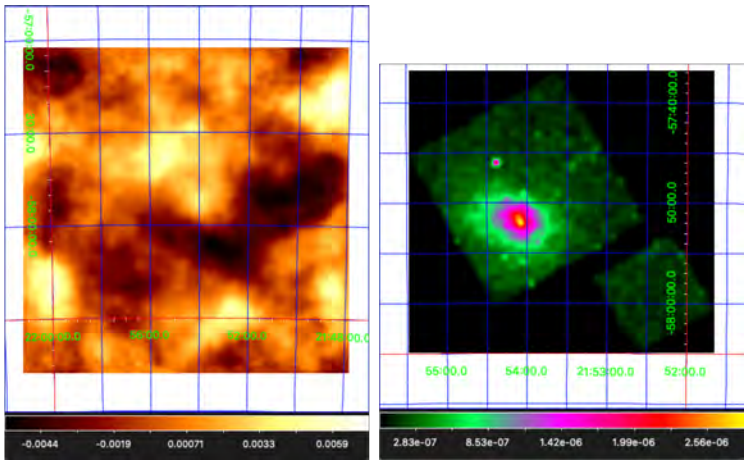

Figure 8: Shown on the left is the produced convergence map for cluster A3822 and on the right is the cluster's x-ray images obtained from the Chandra observatory.

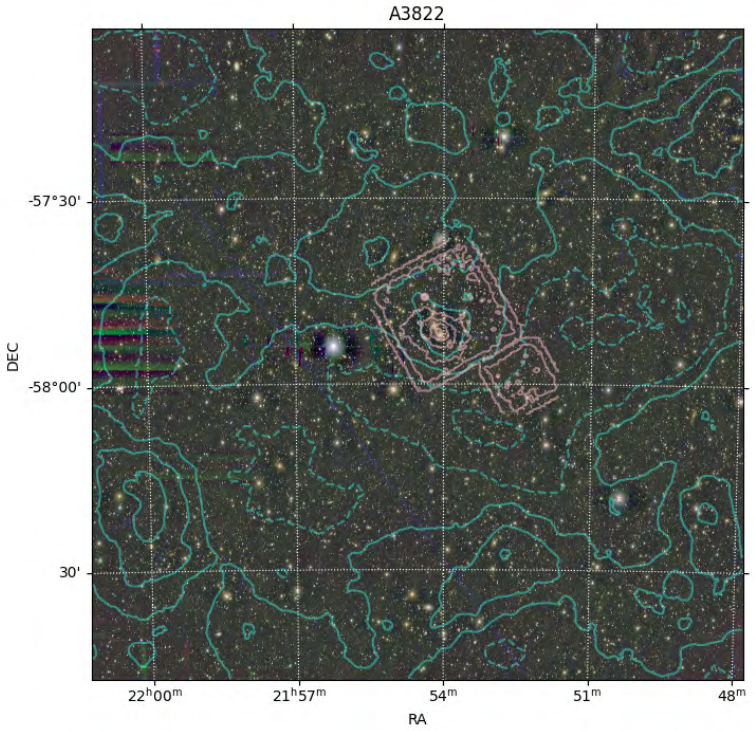

Figure 9: Shown are x-ray contours in pink and mass density contours in blue, overlaid on an irg color image of cluster A3822.

lines up with the x-ray determined cluster center is much lower than the surrounding areas of mass density. We would expect the opposite to be true, even if concentrations of dark matter (DM) were present. In an ideal case, we could use the convergence contours to help better quantify the location and extendedness of DM present in galaxy clusters, however, more rigorous analysis would need to be performed on A3822 before any conclusions can be drawn. In Appendix A, the same plots are shown for clusters A2457, A3827, A3667, and A3695.

4.2 Shear Profiles

We can plot the ellipticity of background galaxies as a function of cluster radius as a proxy to study the shear profile. Shown in figure 10 is the shear profile of A3822 where the blue line plots the tangential component of the ellipticity and the orange line plots the cross component of the ellipticity. The cross component should be unaffected by lensing, should remain around zero, and was included as a quality test. The tangential component on the other hand, should be dependent on lensing. Thus, we expect the tangential component to be strongest near the cluster center at low radii and decrease moving out. In green is the shear profile as would be produced by a cluster with a NFW profile with a total mass of best fit. The ellipticity data points include error bars which are the statistical error caused by the shapes of the background galaxies, given by $\sigma_\epsilon = \bar{\epsilon}\frac{1}{\sqrt{n}}$, where $\bar{\epsilon}$ is the average measured ellipticity at that radius and n is the number of lensed objects.

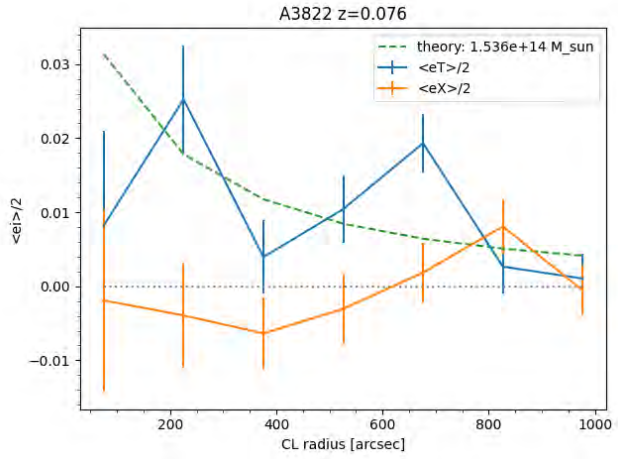

Figure 10: Plotted is the ellipticity as a function of radius for cluster A3822, which is analogous to a shear profile. In blue is the tangential component of the ellipticity and in orange is the cross component. In green is the model NFW profile with a best-fitted mass.

The shear profiles for clusters A2457, A3827, A3667, A3695, A3376, A1650, and A3266 can be found in Appendix A. For most of the clusters, we see that the model NFW profile is within the error bars of the tangential ellipticity, with the notable exceptions being A3822 (figure 10) and A3695 (figure 19). In the case of A3822, this noise in the shear profile could be a result of the noise in the outer edges of the convergence map discussed previously.

As for A3695, one possible explanation for the noise in the shear profile could be due to the fact that it is in a gravitationally bound system with cluster A3696 (α: 20^h 35^m 10^s and

δ: $-34^\circ\ 54'\ 36''$). Since our model only takes as input one cluster center which was chosen based on the x-ray images, the shearing due to the center of A3696 may be contributing to this variation seen in the tangential ellipticity around the center of A3695.

4.3 X-ray Mass vs Lensing Mass

By plotting the cluster masses obtained via their x-ray luminosities as a function of the cluster masses obtained through lensing analysis (shown in table 2), we can hopefully arrive at some kind of scaling relation. This is shown in figure 11. It should be noted that the x-ray masses were based on the assumption that the background galaxies all have $z \approx 0.8$. In reality, the mean redshifts are much less, meaning the resulting lensing masses are lower limit approximations. This being said, their relative differences should be unaffected and any scaling relation will just be scaled by some additional factor.

Name	$M_{x\text{-}ray}$ $[M_\odot]$	$M_{lensing}$ $[M_\odot]$
A3822	3.04990e+14	1.54e+14
A2457	1.81940e+14	0.96e+14
A3827	4.58900e+14	3.45e+14
A3667	5.16960e+14	1.45e+14
A3695	3.72970e+14	1.65e+14
A3376	1.97610e+14	0.83e+14
A0085	5.31630e+14	1.43e+14
A1650	3.35580e+14	1.61e+14
A3266	3.35580e+14	1.46e+14

Table 2: Shown are the x-ray luminosity masses and lensing masses.

In figure 11, it is difficult to infer a numerical relation since this study only includes 9 clusters. However, qualitatively, a positive correlation is quite apparent. It is also reassuring that the clusters with similar x-ray masses also have very similar lensing masses. For example, A3695 (in pink), A1650 (in black), A3822 (in blue), and A3266 (in yellow), are all close together suggesting. This being said, clusters A0085 (in gray) and A3667 (in green) have similar lensing masses as the clusters just mentioned, however, their x-ray masses exceeds the other clusters. This could be hinting at the clusters underlying physical properties which the x-ray mass would be affected by but the lensing mass would not.

Although the mass-luminosity relation is an empirical one, certain clusters can deviate from this relation. In particular, clusters whose intergalactic gas has been heated by mechanisms other than gravitational infall are known to deviate [8]. Furthermore, for smaller and cooler clusters this additional heating has a larger effect. We could investigate this factor further if we had a larger range of cluster x-ray masses, however, for now, it is sufficient to accept this as a factor contributing to the spread in x-ray mass.

We see far less scatter in the lensing mass when looking at the groupings of data points. This is reassuring and alludes to the fact that the lensing mass does not rely on the physical state of the cluster. The scatter that we do see, as mentioned previously, could be explained by the viewing angle and projection effects. This could be a contributing factor with A3827.

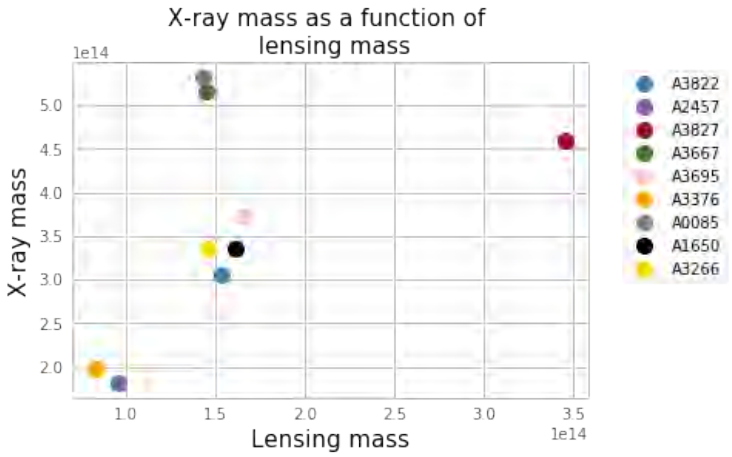

Figure 11: Plotted is the x-ray mass as a function of the lensing mass. Ideally, we expect to see a scaling relation, however due to the small number of clusters that were investigated, a positive correlation between the two can only be qualitatively noticed. It is also important to note that the x-ray mass and lensing mass each contain intruinsic scatter in their measurements, which also explains the vertical and horizontal noise in the data points.

5 Concluding Remarks

This study involved an investigation using weak gravitational lensing as a technique to probe the mass characteristics of galaxy clusters, and then the obtained lensing masses were compared to the x-ray luminosity mass. First, the general geometry of weak lensing was introduced and then relevant methods of obtaining cluster masses were detailed. In the methodology, we outlined the LSST pipeline and discussed the processes involved in producing convergence maps and shear profiles. Lastly, the results of the data were discussed, as well as a brief description of possible sources of error.

5.1 Sources of Error

Since this project was methodology-heavy, error could have been introduced at any step, making it difficult to quantify the error entirely. For this reason, we will briefly outline the possible and most significant sources of error. Starting from the beginning, the exposure images could be affected by telescope focus or atmospheric effects. Throughout the LSST pipeline, factors could introduce noise including variation in the PSF, failure in the CCD bias subtraction, stacking misalignment, and accuracy of galaxy shape measurements. There is also noise present in the convergence maps and shear profiles. Both of these plots will be affected by the random shape noise of the sources and the convergence map will intrinsically contain more noise since it is generating more data points via shear measurements. The shear profiles could also suffer from the uncertainty in the chosen cluster center coordinates, especially if there are two central regions like in the case of A3695. In addition, all quantities derived from lensing analysis would be affected by the inclusion of unlensed cluster memeber galaxies into the set of background galaxies, leading to an underestimation of the mass concentration. The uncertainty in the NFW profile fit and in the total lensing masses

can be attributed to the $z \approx 0.8$ value chosen for the background galaxies. Lastly, when looking at the mass-observable relation between the x-ray mass and lensing mass, sources of error exist for both quantities. The causes of spread in the lensing mass have been discussed and include triaxial viewing angle projection effects which can lead to over and under-estimates by a factor of two in mass concentration measurements [2]. In addition, the lensing-determined mass distribution is affected by the matter between the source, lens, and observer which may add or subtract the amount of observed shear signal. As for the x-ray mass, this assumes that the cluster is virialized and more strictly, that it is in hydrostatic equilibrium and could easily be effected by cluster rotation, magnetic field pressure, or random gas motion on a cluster-to-cluster basis [8].

5.2 Future Steps

Some short-term goals for future analyses include reproducing shear profiles for the clusters with more accurate background galaxy redshifts. This would also help to improve the lensing mass measurements. In addition, it would be useful to strategize a method of estimating the error of each clusters x-ray luminosity mass and lensing mass. This investigation could be done with the cluster data that is already available but would likely involve reviewing the present literature on these individual clusters and other studies' methods to estimate error in lensing mass and/or x-ray luminosity mass.

All of the above discussed sources of error further emphasize the need for the inclusion of more clusters in this analysis. Not only would an increased number give the x-ray mass and lensing mass scaling relation more data points and thus more significance, it could yield more insight into what factors are introducing the most error.

This will require the continued collaborative efforts of the members of the Gravitational Lensing Group at Brown University. However, with each new cluster analyzed, we are one step closer to accomplishing the specific goal of calibrating the mass-observable relation. In the grand scheme of things, however, we will be one step closer to understanding the matter distributions of the largest gravitational structures in the universe, probing dark matter, and constraining the cosmological parameters which describe the evolution and existence of the universe.

6 Acknowledgements

I am extremely grateful to Ian for being a wonderful advisor and for being incredibly supportive and kind. I also want to thank Shenming for all of his one-on-one help he has offered and for the troubleshooting he has aided with over many emails. Lastly, I would like to thank Claire and Nick for providing technical and moral support throughout this project.

References

[1] S. W. Allen, R. W. Schmidt, and A. C. Fabian. Cosmological constraints from the X-ray gas mass fraction in relaxed lensing clusters observed with Chandra. , 334(2):L11–L15, August 2002.

[2] Virginia L. Corless and Lindsay J. King. A statistical study of weak lensing by triaxial dark matter haloes: consequences for parameter estimation. , 380(1):149–161, September 2007.

[3] Shenming Fu and Ian Dell'Antonio. LSST Science Pipelines obs decam Tutorial. Unpublished, 2019.

[4] C. S. Kochanek, Martin White, J. Huchra, L. Macri, T. H. Jarrett, S. E. Schneider, and J. Mader. Clusters of Galaxies in the Local Universe. , 585(1):161–181, March 2003.

[5] Jacqueline McCleary, Ian dell'Antonio, and Anja von der Linden. Dark Matter Distribution of Four Low-z Clusters of Galaxies. , 893(1):8, April 2020.

[6] Nobuhiro Okabe, Masahiro Takada, Keiichi Umetsu, Toshifumi Futamase, and Graham P. Smith. LoCuSS: Subaru Weak Lensing Study of 30 Galaxy Clusters. , 62:811, June 2010.

[7] R. Piffaretti, M. Arnaud, G. W. Pratt, E. Pointecouteau, and J. B. Melin. The MCXC: a meta-catalogue of x-ray detected clusters of galaxies. , 534:A109, October 2011.

[8] P. Schneider. *Extragalactic astronomy and cosmology: An introduction*. 01 2006.

[9] Peter Schneider, Jürgen Ehlers, and Emilio E. Falco. *Gravitational Lenses*. 1992.

[10] A. Vikhlinin, A. Kravtsov, W. Forman, C. Jones, M. Markevitch, S. S. Murray, and L. Van Speybroeck. Chandra Sample of Nearby Relaxed Galaxy Clusters: Mass, Gas Fraction, and Mass-Temperature Relation. , 640(2):691–709, April 2006.

[11] Joachim Wambsganss. Gravitational Lensing in Astronomy. *Living Reviews in Relativity*, 1(1):12, December 1998.

[12] David Wittman. *Weak Lensing*, volume 608, page 55. 2002.

7 Appendix A

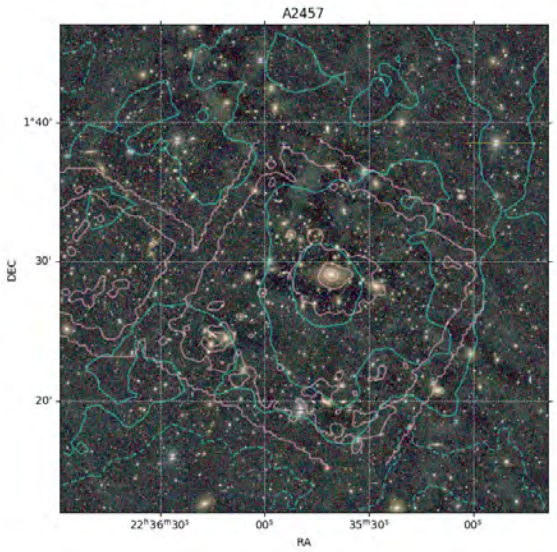

Figure 12

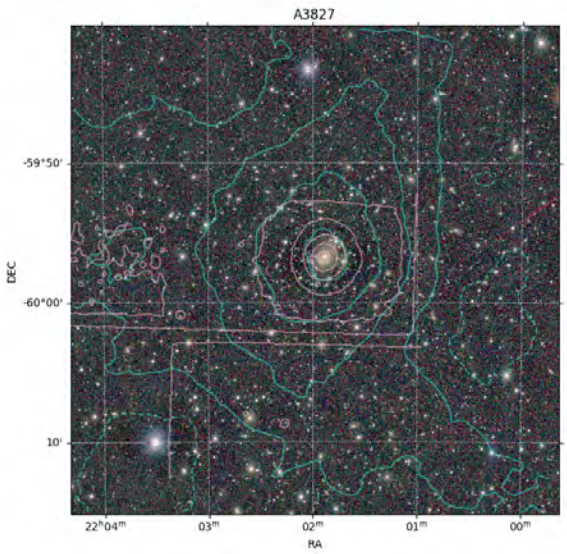

Figure 13

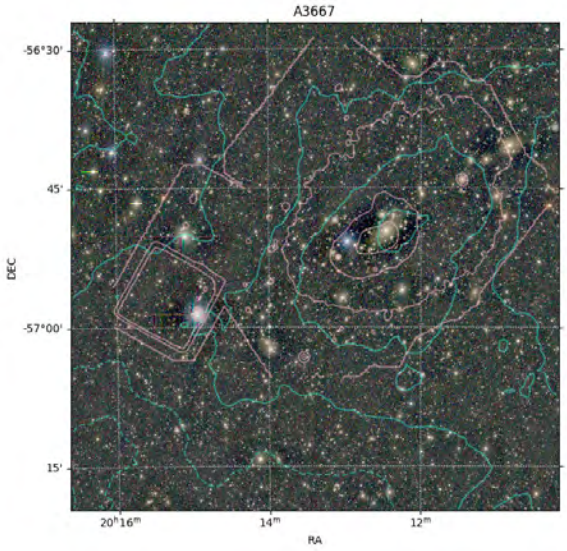

Figure 14

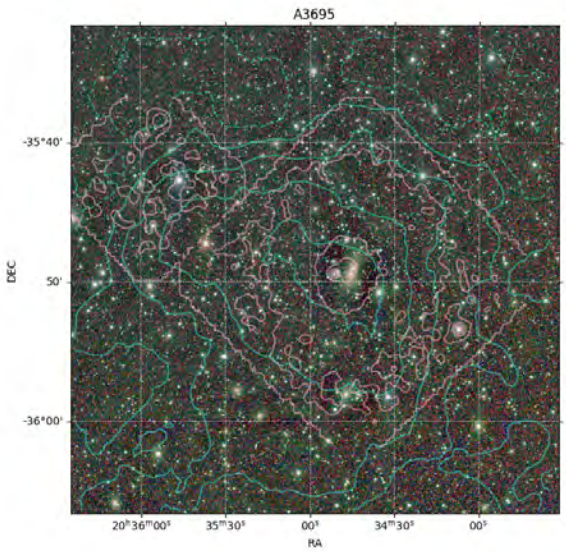

Figure 15

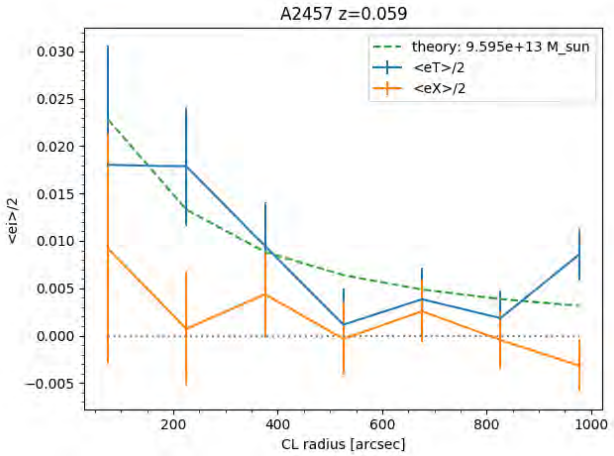

Figure 16

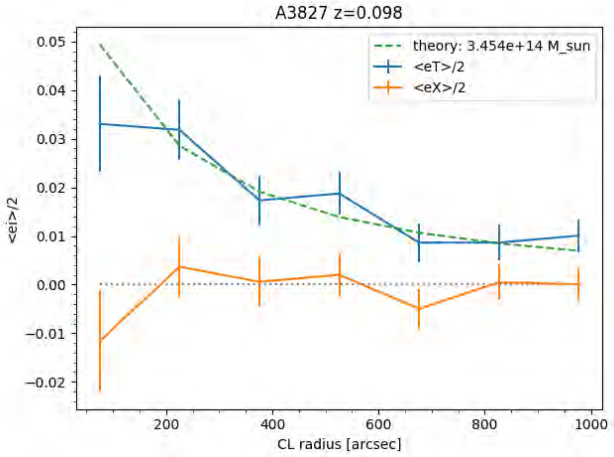

Figure 17

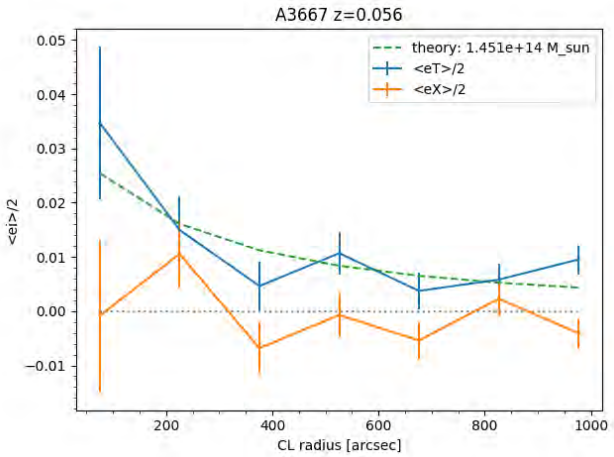

Figure 18

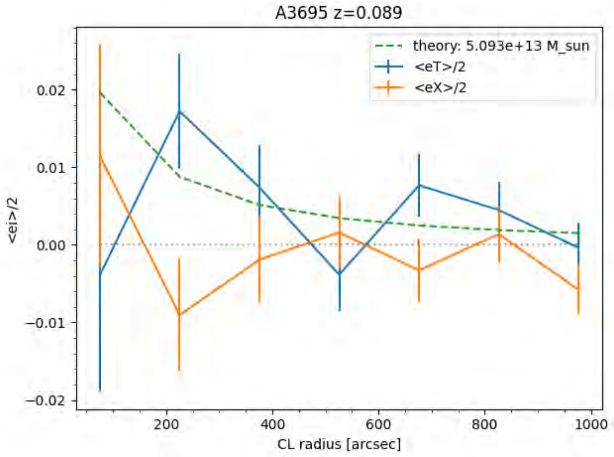

Figure 19

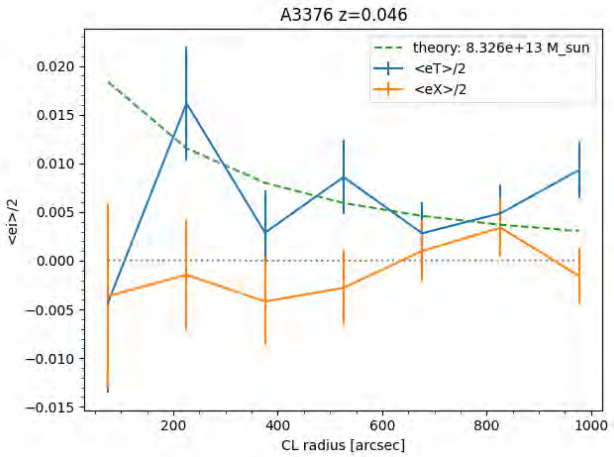

Figure 20

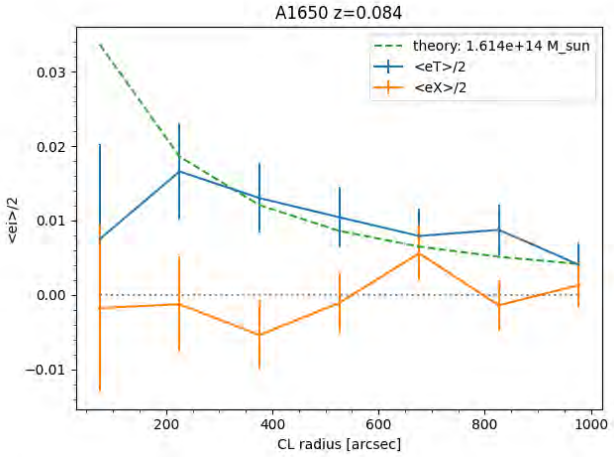

Figure 21

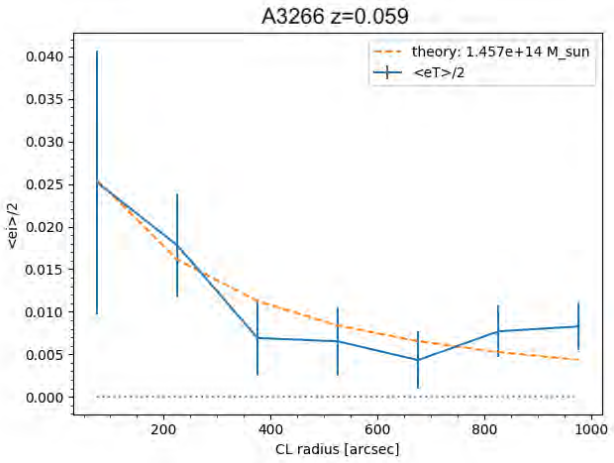

Figure 22